Sound & Vibration 2026, 60(4), 4256.
doi: https://doi.org/10.59400/sv4256

Article

Adaptive decomposition and energy-frequency characteristics of high-speed railway train vibration signals on the surface of shallow-buried tunnels

Linli Zhou[1,*], Kenan Zheng[1], Baoxin Jia[1,2], Zhiyang Zhou[1], Sihao Ding[1]

[1] School of Civil Engineering, Liaoning Technical University, Fuxin 123000, China

[2] Liaoning Key Laboratory of Ecological Restoration Technology in Abandoned Mining Areas, Liaoning Technical University, Fuxin 123000, China

*** Corresponding author:** Linli Zhou, larryzll@163.com

CITATION

Zhou L, Zheng K, Jia B, et al. Adaptive decomposition and energy-frequency characteristics of high-speed railway train vibration signals on the surface of shallow-buried tunnels. Sound & Vibration. 2026; 60(4): 4256. https://doi.org/10.59400/sv4256

ARTICLE INFO

Received: 12 April 2026
Revised: 6 May 2026
Accepted: 12 May 2026
Available online: 20 July 2026

Abstract: Vibration signals induced by high-speed railway trains on the surface above shallow-buried tunnels exhibit strong non-stationarity and high background noise due to the coupling of tunnel dynamic response and environmental noise. Traditional signal processing methods struggle to extract key wheel-rail vibration components accurately. To solve this issue, this study proposes an adaptive parameter optimization method for variational mode decomposition (VMD), termed SE-SSA-VMD, based on sample entropy (SE) and the sparrow search algorithm (SSA). By intelligently optimizing the mode number K and penalty factor α, the method improves decomposition objectivity and anti-noise robustness. Simulation results confirm that the method achieves accurate effective mode separation with an average center frequency error below 0.2 Hz at a signal-to-noise ratio of 5 dB. Measured data indicate that vibration energy is mainly concentrated in 35–60 Hz with a Gaussian unimodal distribution, and the adjusted R^2 of over 95% measuring points exceeds 0.8. Higher train speed significantly increases vertical vibration energy, while longer marshalling mainly strengthens lateral vibration energy; both cause a downward shift of the dominant frequency. Far-field vibration energy does not decay monotonically and shows slight local fluctuations, but remains at a low level owing to strong energy dissipation of overlying artificial fill, regardless of initial speed and near-field energy. This work provides an effective approach and theoretical support for vibration assessment and mitigation design in shallow-buried high-speed railway tunnel sections.

Keywords: shallow-buried tunnel; high-speed railway train vibration signal; energy-frequency characteristic; variational mode decomposition; parameter adaptation; energy attenuation

1. Introduction

The rapid development of high-speed railways has greatly improved transportation efficiency, but it has also caused widespread vibration impacts along railway corridors. This long-term vibration not only affects the living environment of surrounding residents but also reduces the service safety performance of structures [1–3]. Therefore, clarifying the excitation mechanism and propagation characteristics of such vibrations is a prerequisite for engineering scientific issues such as environmental vibration impact prediction, assessment, control, and site detection of high-speed railways. Affected by environmental factors, the high-speed railway train vibration signals collected on-site are usually accompanied by a certain degree of noise. The main sources of this noise include two aspects: one is the noise sources around the collection location, such as residential areas, factories, and vehicles; the other is the engineering structures around the collection location that are prone to continuous dynamic responses, such as long tunnels and large-span buildings. Relevant studies have shown that, compared with the subgrade site of bridge lines, the overlying surface of shallow-buried tunnels has a significant increase in noise content by more than 30% due to the continuous dynamic response of the tunnel structure (long-span, closed space), leading to deep superposition of noise and train vibration signals [4, 5]. Under such a high-noise environment, the effective components of vibration signals (such as the main frequency band of 30-60 Hz reflecting wheel-rail interaction) are easily interfered with or masked. Khan and Dasaka [6] investigated the characteristics of ground vibration induced by high-speed trains and clarified that railway vibration propagating in the stratum is transmitted to adjacent buildings through the railway embankment and underlying supporting ground. Li et al. [7] studied the dynamic response and vibration impact of the Probhutaratna pagoda in the suburbs of Beijing under train-induced excitation. Lei et al. [8] investigated the vibration characteristics of subway turnout areas during train deceleration, processing vibration signals via wavelet analysis and the 2D kernel density algorithm, and establishing a multi-scale vehicle-turnout-tunnel-soil coupled vibration model verified with test data. Yi et al. [9] analyzed the characteristics of vibration source intensity in turnout zones as well as the practical vibration reduction performance of different vibration mitigation measures. Therefore, effective noise reduction and feature extraction of vibration signals are the reliability guarantee for subsequent vibration impact assessment and vibration reduction measure design.

Currently, there are obvious limitations in the processing and feature extraction methods of high-speed railway train vibration signals on the overlying surface of shallow-buried tunnels. In terms of time-frequency analysis technology, methods such as the Short-Time Fourier Transform (STFT) [10] and the Synchrosqueezed Wavelet Transform (SWT) [11] can initially extract the energy-frequency information of signals. However, STFT is limited by the selection of fixed window length. If the window length is too short, it is impossible to separate high-frequency noise from effective modes; if the window length is too long, the time-domain resolution will decrease, making it impossible to accurately reflect the transient characteristics of signals. Although SWT improves time-frequency aggregation through rearrangement technology, it is affected by instantaneous frequency estimation errors and interference points during the rearrangement process, which may easily misjudge the resonance noise of the tunnel structure as effective vibration components. Mode decomposition technology can decompose complex vibration signals into sub-modes with single-frequency characteristics, realizing deep separation of noise and effective components. Empirical Mode Decomposition (EMD) [12, 13] and Empirical Wavelet Transform (EWT) [14] are widely used technical methods. However, considering the actual characteristics of signals on the overlying surface of shallow-buried tunnels, both still have obvious adaptation defects. Although EMD can adaptively decompose signals, it is prone to mode mixing under the influence of signal non-stationarity, and the end effect will further aggravate the decomposition deviation. EWT is affected by the uneven distribution of signal spectrum amplitude, which may easily lead to sparse segmentation of the effective frequency band of vibration signals and fail to completely retain the core modes of wheel-rail vibration. To address the shortcomings of the above mode decomposition methods, Dragomiretskiy and Zosso [15] proposed Variational Mode Decomposition (VMD) based on the principle of EMD. This method constructs a variational analysis model centered on signal frequency information and has stronger noise robustness [16]. Considering that the decomposition effect of VMD is highly dependent on the selection of the number of modes K and penalty factor α, relevant scholars have successively proposed methods such as the center frequency observation method [17,18], index construction optimization [19], and Particle Swarm Optimization (PSO) [20–22] to realize the optimal selection of the number of VMD modes, and combined traditional indicators such as Sample Entropy (SE) and Envelope Entropy (EE) as the core fitness functions for parameter optimization.

In summary, existing methods such as PSO-VMD can mitigate the subjectivity of manual selection of VMD parameters to a certain extent. However, relevant literature indicates that their optimization results are still susceptible to the initial particle distribution and local extremum. In contrast, the Sparrow Search Algorithm (SSA) possesses superior performance in global search capability, convergence stability, and the ability to escape local optima. Sample Entropy (SE) can characterize the variations in complexity and self-similarity of non-stationary signals, making it suitable as an evaluation indicator for the decomposition quality of noisy vibration signals. On this basis, this paper proposes an adaptive VMD parameter optimization method integrating Sample Entropy (SE) and the Sparrow Search Algorithm (SSA), termed SE-SSA-VMD. The method jointly determines the mode number K and penalty factor α of VMD, so as to achieve accurate separation of key components such as wheel–rail interaction from high-speed railway vibration signals. Furthermore, combined with on-site monitoring tests, the energy-frequency distribution characteristics of vibration signals under different train speeds and marshalling conditions and their attenuation laws during propagation are systematically analyzed. The prominent innovations of this paper are as follows: taking sample entropy as the fitness function, using the sparrow search algorithm to perform global automatic optimization of the key parameters of VMD, which effectively overcomes the human dependence and mode mixing problems in traditional methods, and improves the objectivity and reliability of extracting effective wheel-rail vibration components from a strong noise background. For the first time, the coupling influence mechanism of speed and marshalling on the vibration energy frequency and propagation law of the shallow-buried tunnel surface is quantitatively revealed. It is clarified that increasing speed mainly sharply increases vertical vibration energy, while increasing marshalling mainly strengthens lateral vibration energy. It is also found that both lead to a shift of the main vibration frequency to lower frequencies, and the far-field energy is sharply attenuated due to the dominant effect of strong dissipation of the overlying soil. The research results can provide a reference for the processing of field vibration monitoring data in shallow-buried tunnel sections, the evaluation of key frequency bands in sensitive areas, and the selection of target frequency bands for vibration reduction measures.

2. VMD and parameter adaptive optimization

2.1. Principle of VMD

VMD is a fully non-recursive signal decomposition method with an adaptive solution. It converts mode estimation into a variational problem, and then finds the optimal solution of the constrained variational model through iterative search. Its function is to decompose the real-valued input signal f into a finite number of sub-signals u_k, and each mode has its own center frequency ω_k.

First, the mode function is defined as an amplitude-modulated and frequency-modulated signal, expressed as Equation (1) [15]:

$$u_k(t) = A_k(t)\cos\left(\varphi_k(t)\right) \tag{1}$$

Where, $u_k(t)$ is the sub-signal after VMD decomposition; $A_k(t)$ is the instantaneous amplitude of the sub-signal, $A_k(t) \geq 0$; $\varphi_k(t)$ is the instantaneous phase of the sub-signal, which is a non-decreasing function, $\varphi'_k(t) \geq 0$; $\omega_k(t) = \varphi'_k(t)$ is the center frequency of the sub-signal.

Then, the Hilbert transform is performed on the mode u_k, the transformed spectrum is shifted to the baseband according to the estimated center frequency, and the square of the L2 norm of its gradient is taken to estimate the bandwidth, thereby establishing a constrained variational model. To ensure the convergence of the model and the strict implementation of constraints, a penalty factor α and a Lagrange multiplier λ are introduced to reconstruct the original constrained variational problem into an unconstrained variational problem. The expression of the augmented Lagrange function $\mathcal{L}$ is shown in Equation (2) [15]:

$$\begin{gathered}\mathcal{L}(\{u_k\},\{\omega_k\},\lambda) = \\ \alpha\sum_k \left\|\partial_t\left[(\delta(t)+\tfrac{j}{\pi t})*u_k(t)\right]\times e^{-j\omega_k t}\right\|_2^2 + \left\|f(t)-\sum_k u_k(t)\right\|_2^2 \\ +\left\langle\lambda(t), f(t)-\sum_k u_k(t)\right\rangle\end{gathered} \tag{2}$$

Where, $\{u_k\} = \{u_1, \ldots, u_k\}$ represents the set of all modes; $\{\omega_k\} = \{\omega_1, \ldots, \omega_k\}$ represents the center frequency corresponding to each mode; $\delta(t)$ is the Dirac function; * is the convolution symbol; $f(t)$ is the real-valued input signal; the constraint condition is that the sum of each mode is equal to the input signal; α is the penalty factor; $\lambda(t)$ is the Lagrange multiplier.

By solving the optimal solution of the above variational model, i.e., the saddle point of the augmented Lagrange function $\mathcal{L}$, the mode u_k can be obtained as shown in Equation (3) [15]:

$$\widehat{u}_k^{n+1}(\omega) = \frac{\widehat{f}(\omega) - \sum_{i^1 k}\widehat{u}_i(\omega) + \frac{\widehat{\lambda}(\omega)}{2}}{1+2\alpha(\omega-\omega_k)^2} \tag{3}$$

Where, $\widehat{u}_k^{n+1}(\omega)$, $\widehat{f}(\omega)$, $\widehat{u}_i(\omega)$, $\widehat{\lambda}(\omega)$ are the Fourier transforms of $u_k^{n+1}(t)$, $f(t)$,

$u_i(t)$, $\lambda(t)$ respectively; n is the iteration step. By performing the inverse Fourier transform on the obtained $\widehat{u}_k(\omega)$ and taking its real part, the time-domain mode $u_k(t)$ is obtained.

2.2. Sparrow search algorithm (SSA)

The number of modes K and the penalty factor α in VMD dominate the result of signal decomposition. The number of modes K determines the number of modes obtained by decomposition. A K value that is too small leads to insufficient signal decomposition and failure to obtain effective components of the signal; whereas a K value that is too large causes over-decomposition and is prone to mode mixing. The penalty factor α is inversely proportional to the bandwidth of the mode component. An inappropriate value may also cause mode mixing in signal decomposition or even failure to complete the signal decomposition process. Since the number of modes and the penalty factor jointly affect the signal decomposition result during the variational mode decomposition process, they need to be optimized together during parameter optimization.

To reduce the influence of human experience on parameter determination during parameter optimization and improve adaptive capacity, SSA is selected for VMD parameter optimization.

SSA is an intelligent optimization algorithm proposed by Xue and Shen [23] that simulates the population behavior and individual behavior of sparrow groups in nature during foraging and avoiding natural enemies.

In the SSA, discoverers with high energy occupy a favorable position for feeding and foraging, can obtain food first, and have a wider sensing range for food-rich areas compared with followers. During the position update iteration process, the position of the discoverer is shown in Equation (4):

$$X_{ij}^{t+1} = \begin{cases} X_{ij}\exp\left(-\frac{i}{\beta \cdot iter_{\max}}\right) & R_2 < ST \\ X_{ij} + QL & R_2 \geq ST \end{cases} \tag{4}$$

Where, T represents the current iteration number; $iter_{\max}$ represents the maximum number of iterations; X_{ij} represents the position information of the i-th sparrow in the j-th dimension; $\beta \in (0,1]$ represents a random number; R_2 represents the early warning value, with a value range of [0,1]; ST represents the safety value, with a value range of [0.5,1]; Q represents a random number following a normal distribution; L represents a $1 \times d$ matrix with all elements being 1.

For followers, when a follower finds that the discoverer it follows has found a new foraging ground, it will immediately leave its current position to compete for food at that location. The position of the follower is shown in Equation (5):

$$X_{ij}^{t+1} = \begin{cases} Q\exp\left(\frac{X_{\text{worst}} - X_{ij}^{t}}{i^2}\right) & i > \frac{n}{2} \\ X_P^{t+1} + |X_{ij} - X_P^{t+1}|LA^{+} & i \leq \frac{n}{2} \end{cases} \tag{5}$$

Where, X_P represents the best position of the discoverer in the current population; X_{worst} represents the worst position of the follower in the current population; A is a $1 \times d$ matrix with elements randomly assigned to 1 or −1, and $A^{+} = A^{T}(AA^{T})^{-1}$.

While the sparrow group is foraging, some individuals will take on the responsibility of vigilance. When an individual in the population detects danger and issues an alarm, the individuals in the population will move to a safe position. The position update is shown in Equation (6):

$$X_{ij}^{t+1} = \begin{cases} X_{\text{best}}^t + \beta |X_{ij}^t - X_{\text{best}}^t| & f_i > f_b \\ X_{ij}^t + \kappa (\frac{|X_{ij}^t - X_{\text{worst}}^t|}{(f_i - f_w) + \varepsilon}) LA^+ & f_i = f_b \end{cases} \tag{6}$$

Where, X_{best} represents the best feeding position at the current location; β represents the step size control parameter, a random number following a normal distribution with a mean of 0 and a variance of 1; κ is a random number in the range of [−1,1], representing the moving direction; f_i represents the fitness value of the current sparrow individual; f_{w} represents the worst fitness value in the current population; f_{b} represents the best fitness value in the current population; ε represents a constant to avoid division by zero.

2.3. Sample entropy

In SSA, it is necessary to construct an individual fitness function. In signal analysis and processing, Sample Entropy (SE) can clearly reflect the complexity of time series. The sample entropy of a time series is proportional to its complexity and inversely proportional to its self-similarity. Therefore, sample entropy is used as the fitness function of the SSA algorithm.

For a time series $X = [x_1, x_2, x_3, \ldots, x_{\text{N}}]$ composed of N data points, two similar sequences of length m, and a similarity tolerance r, the calculation process of sample entropy is as follows:

(1) The original time series X is sorted in a certain order to obtain a vector of dimension m, as shown in Equation (7):

$$x_i^m = [x_i^m(1), \cdots, x_i^m(k), \cdots, x_i^m(m)], 1 \leq i \leq N - m + 1 \tag{7}$$

Where, $x_i^m(k) = x(i + k + 1)$, and m is the embedding dimension.

(2) Calculate the relative distance between vectors x_i^m and x_j^m, as shown in Equation (8):

$$d\left[x_i^m, x_j^m\right] = max(|x_i^m(k) - x_j^m(k)|), k = 1, \cdots, m \tag{8}$$

(3) For any i value, calculate the Chebyshev distance between vector x_i^m and the other vectors x_j^m; count the number of d_{ij} less than r and denote it as B_i, then calculate the average value $B^m(r)$ of $B_i^m(r)$, as shown in Equation (9). Repeat the above steps to obtain $B^{m+1}(r)$:

$$B^m(r) = \frac{1}{N - m + 1} \sum_{i=1}^{N-m+1} \frac{B_i}{N - m} \tag{9}$$

(4) The sample entropy expression of the time series is shown in Equation (10):

$$SE(m, r, N) = -ln\left[\frac{B^{m+1}(r)}{B^m(r)}\right] \tag{10}$$

Sample entropy is affected by the embedding dimension *m* and similarity tolerance *r* [24]. Usually, $m = 2$ and $r = (0.1–0.25)\delta_x$ are set, where δ_x is the standard deviation of the original data.

Combining the algorithms in the above 3 sections, taking sample entropy as the fitness function, the sparrow search algorithm is used to optimize the parameter values of variational mode decomposition, realizing the parameter adaptive solution of vibration signal variational mode decomposition, and forming the SE-SSA-VMD parameter adaptive variational mode decomposition method for vibration signals. The decomposition process is shown in **Figure 1**.

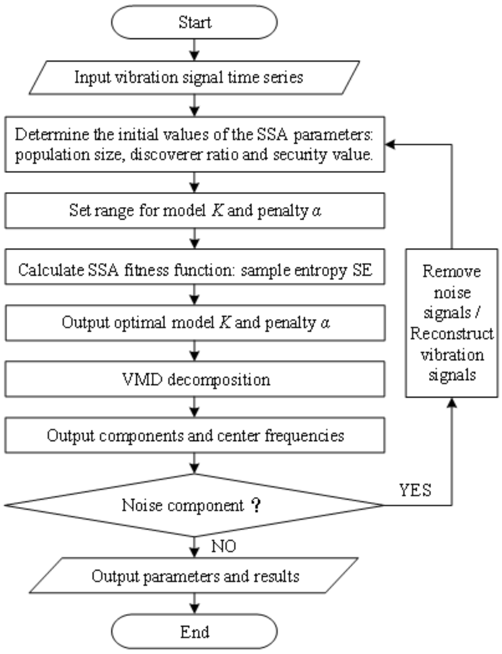

Figure 1. SE-SSA-VMD parameter adaptive decomposition process.

2.4. VMD parameter adaptation

2.4.1. Principle of correlation coefficient

The mode components after VMD decomposition include noise components and useful signal components. To solve this problem, this study constructs a component selection criterion based on the correlation coefficient, aiming to accurately separate and retain effective signal components by quantitatively analyzing the correlation between each mode component and the original signal, i.e., the correlation coefficient C_i. The expression is shown in Equation (11):

$$C_i = \frac{\sum\left(\varepsilon_i - \overline{\varepsilon_i}\right)\left(\varphi - \overline{\varphi}\right)}{\sum\left(\varepsilon_i - \overline{\varepsilon_i}\right)^2 \sum\left(\varphi - \overline{\varphi}\right)^2} \tag{11}$$

Where, ε_i is each mode component obtained by decomposition; φ is the original input signal; $\bar{\varepsilon}_i$ is the average value of the mode component; $\bar{\varphi}$ is the average value of the original input signal.

The calculation formula of the threshold C_η is shown in Equation (12):

$$C_\eta = \frac{\varepsilon_{\max}}{10\varepsilon_{\max} - 5} \tag{12}$$

Where, $\varepsilon_{\max}$ is the maximum value of the mode component correlation coefficient.

2.4.2. Analog signal simulation and verification

To verify the effectiveness of SE-SSA optimization, an analog signal of high-speed railway train wheel-rail force composed of superposed harmonic waves with different frequencies is constructed for verification. The simulation formula of the high-speed railway train wheel-rail force signal is shown in Equation (13) [25]:

$$F(t) = k_1 k_2 \left(F_0 + F_1 sin\, \omega_1 t + F_2 sin\, \omega_2 t + F_3 sin\, \omega_3 t\right) \tag{13}$$

Taking the wheel-rail signal generated by the CRH380BG high-speed train running at 300 km/h as an example, k_1 = 1.538, k_2 = 0.7; ω_1 = 16.67π, ω_2 = 83.33π, ω_3 = 333.32π. F_0 = 70 kN, $F_1 = 3.5{\omega_1}^2$, $F_2 = 2{\omega_2}^2$, $F_3 = 0.5{\omega_3}^2$ [25]. The sampling frequency *fs* of the analog signal is 1,000 Hz, and the signal duration t is set to 4 s. The time-domain and frequency-domain diagrams of the analog signal are shown in **Figure 2a**,**b**. The high-speed railway train vibration signals in actual scenarios are also mixed with noise signals. To make the analog signal close to the real collected signal, a set of Gaussian white noise with a signal-to-noise ratio of 7 dB is randomly added to the analog signal to construct a noisy analog signal. The time-domain and frequency-domain diagrams of the noisy signal are shown in **Figure 2c**,**d**.

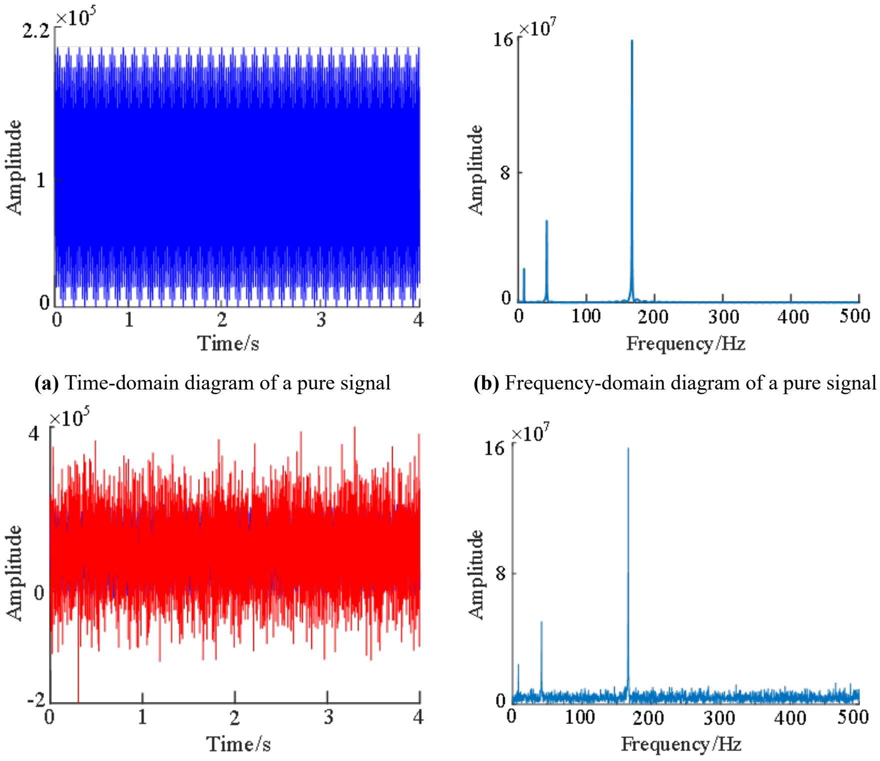

(a) Time-domain diagram of a pure signal **(b)** Frequency-domain diagram of a pure signal

(c) Time-domain diagram of noisy signal **(d)** Frequency-domain diagram of noisy signal

Figure 2. Time- and frequency-domain representations of the signal.

The search ranges of K and α in this paper are determined according to the frequency composition of simulated signals, the physical implications of VMD parameters, and preliminary calculation results. For the simulated signal, the theoretical signal consists of three dominant frequency components; thus, the lower bound of K is set to 3. Considering that additional noise modes may be generated after noise addition and avoiding excessive decomposition, the upper bound of K is set to 15. The penalty factor α controls the bandwidth of each mode. An excessively small α tends to cause an overly wide mode frequency band and subsequent mode mixing, while an excessively large α may lead to mode splitting and the loss of broadband transient features of train-induced vibration signals. Accordingly, its range is set to 100–5,000 based on preliminary trial calculations. For measured high-speed railway vibration signals, their frequency components and noise background are more complex, so the search ranges of K and α are appropriately expanded to improve the adaptability of parameter optimization.

The SE-SSA-VMD optimization parameters of the analog signal are shown in **Table 1**. The optimal number of modes K and penalty factor α searched by SE-SSA are 13 and 3,686, respectively. These parameters are selected to perform SE-SSA-VMD on the analog signal with noise, and the result is shown in **Figure 3a**.

Table 1. SE-SSA-VMD parameters of the analog signal.

Number of sparrow population, n	Proportion of discoverers ratio, PD	Safety value, ST	Range of mode number, K	Range of penalty factor, α
30	0.3	0.7	[3,15]	[100,5,000]

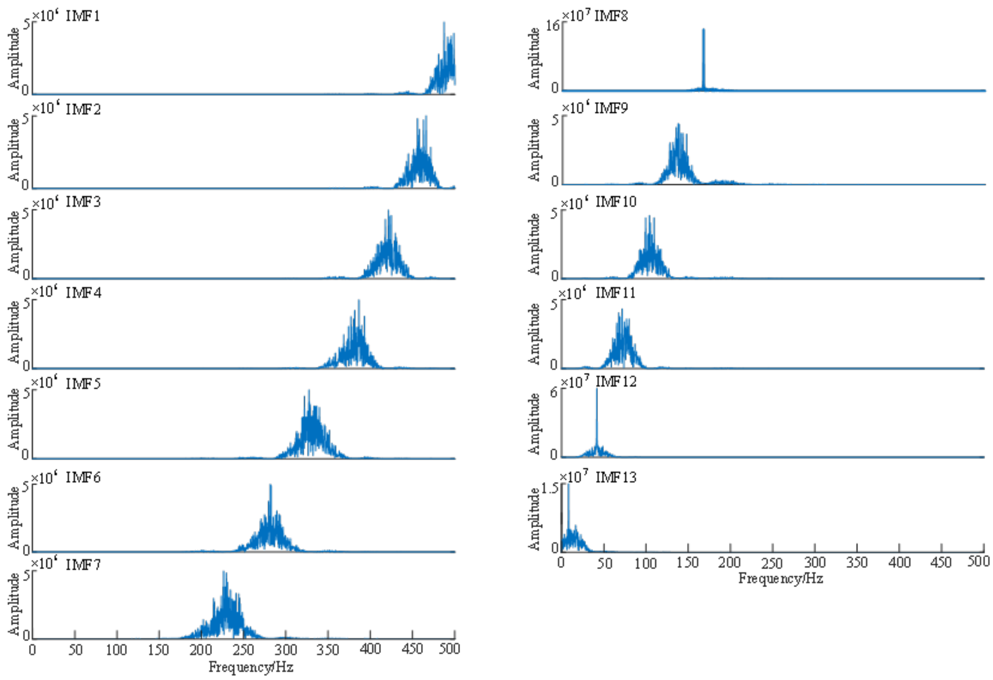

(a) SE-SSA-VMD of an analog signal with noise

Figure 3. *Cont.*

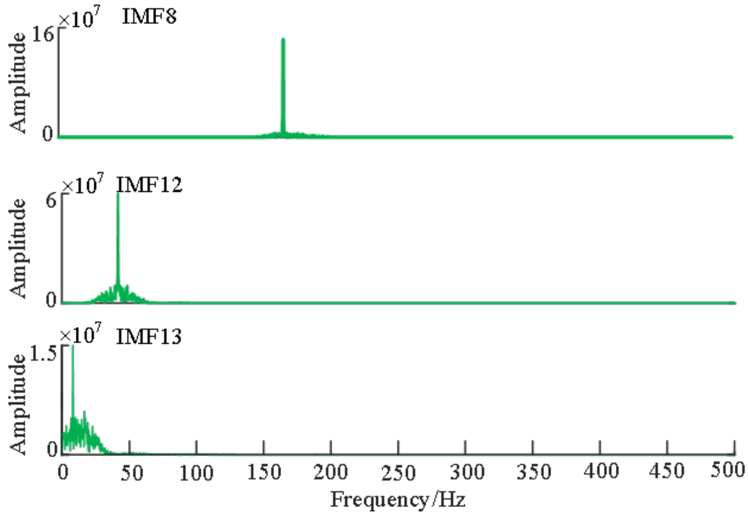

(b) SE-SSA-VMD of useful mode

Figure 3. Signal SE-SSA-VMD.

According to the correlation coefficient and threshold determination formula, noise components and useful components can be distinguished, as shown in **Table 2**. The noise components are discarded, and the useful components are reconstructed to obtain the denoised high-speed railway train vibration signal. Then, SE-SSA-VMD decomposition is performed on the reconstructed high-speed railway train vibration signal again.

Table 2. The correlation coefficient between each mode component and the original signal.

IMF	C_i	C_η	Usefulness or not
1	0.1325	0.244	NO
2	0.1462	0.244	NO
3	0.1672	0.244	NO
4	0.1558	0.244	NO
5	0.1867	0.244	NO
6	0.1595	0.244	NO
7	0.1778	0.244	NO
8	0.8472	0.244	YES
9	0.1985	0.244	NO
10	0.2143	0.244	NO
11	0.1971	0.244	NO
12	0.5567	0.244	YES
13	0.4528	0.244	YES

It can be known from Equation (12) that the threshold is 0.244. The correlation coefficients of IMF8, IMF12, and IMF13 are greater than the threshold, which are useful components; the correlation coefficients of IMF1–IMF7 and IMF9–IMF11 are less than the threshold, which are noise components and are discarded.

The center frequencies of each useful mode of the adaptive decomposition of the analog signal are f_1 = 166.83 Hz, f_2 = 41.76 Hz, f_3 = 8.3 Hz, shown in **Figure 3b**. The center frequencies of the mode components are basically consistent with the main frequencies of each part of the analog signal, and no other frequency modes appear. It indicates that the VMD parameters determined by SE-SSA can accurately decompose the analog signal with noise, and the method is effective.

To further verify the decomposition performance of the SE-SSA-VMD method, decomposition results of EMD, EWT, PSO-VMD, and SE-SSA-VMD are compared under the same simulated signal condition with 7 dB Gaussian white noise. The center frequency of each effective mode for all methods is determined by the spectral peak of the corresponding mode. The center frequency error and mode mixing are adopted as evaluation indices, and the results are listed in **Table 3**.

Table 3. Comparison of decomposition results of different methods for the simulated signal with 7 dB noise.

Method	Identified center frequency 1/Hz	Identified center frequency 2/Hz	Identified center frequency 3/Hz	Average center frequency error/Hz	Maximum center frequency error/Hz	Mode mixing condition
EMD	168.12	43.02	8.92	1.13	1.46	Quite obvious
EWT	165.91	40.84	8.76	0.67	0.83	Certain extent
PSO-VMD	166.97	41.95	8.46	0.24	0.31	Not obvious
SE-SSA-VMD	166.83	41.76	8.30	0.10	0.17	Not obvious

It can be seen from **Table 3** that EMD and EWT suffer from obvious mode mixing or inadequate separation of effective frequency components under noisy conditions. PSO-VMD can mitigate the problem of manual parameter selection, yet its center frequency error is still slightly higher than that of SE-SSA-VMD. In comparison, the center frequencies of effective modes identified by SE-SSA-VMD are much closer to the theoretical values, indicating that the proposed method achieves superior decomposition accuracy and noise immunity.

2.4.3. Stability verification under different signal-to-noise ratios

To further verify the decomposition stability of the SE-SSA-VMD method under different noise levels, Gaussian white noise with different signal-to-noise ratios (SNRs) was added to the original wheel–rail force simulated signals. Analysis was then carried out following the same parameter optimization and mode decomposition procedures. The center frequencies of effective modes and their relative errors were adopted as evaluation indicators, and the results are presented in **Table 4**.

Table 4. Decomposition results of SE-SSA-VMD under different SNR conditions.

SNR/dB	Identify the center frequency 1/Hz	Identify the center frequency 2/Hz	Identify the center frequency 3/Hz	Average center frequency error/Hz	Maximum center frequency error/Hz	Effective mode identification status
5	166.91	41.89	8.23	0.19	0.25	Full Recognition
7	166.83	41.76	8.30	0.10	0.17	Full Recognition
10	166.73	41.70	8.32	0.03	0.07	Full Recognition
15	166.69	41.68	8.33	0.01	0.03	Full Recognition

It can be observed from **Table 4** that SE-SSA-VMD can accurately identify the main frequency components of simulated signals under various SNR conditions, with overall small center frequency errors. No obvious loss of effective modes or severe mode aliasing occurs, which demonstrates that the proposed method possesses excellent decomposition stability and noise immunity under different noise levels.

3. Monitoring and adaptive decomposition of high-speed railway train vibration signals

3.1. High-speed railway train vibration signal monitoring test

The overlying surface of the Koumo Tunnel on China's Beijing-Harbin High-Speed Railway is selected for the vibration monitoring test. The Koumo Tunnel has a total length of 2.47 km, which is currently the longest cut-and-cover tunnel in China. The test site is located at DK541 + 235 of the tunnel. This section of the tunnel is a frame-type lining structure, and the overlying soil of the lining is mainly artificial fill. The test uses the Atenna-4.22 microseismometer for observation and data collection, which mainly includes a microseismic data collector, a gain amplifier, a three-component microseismic sensor, a power controller, a GPS antenna, and a Wi-Fi antenna. The maximum measurement range is 0.5 mm/s, the flat response frequency range is 5–1,000 Hz, and the sampling frequency is set to 10 kHz [1].

In the test site, the layout line of the sensors is perpendicular to the tunnel line. A total of 5 sensors are installed, namely S1–S5 sensors. Among them, the S5 sensor is located on the tunnel center line, and the S1–S4 sensors are located on the north side of the tunnel center line. The three-component sensors are leveled before data acquisition. Their X-direction is perpendicular to the high-speed railway track, the Y-direction is parallel to the high-speed railway track, and the Z-direction is vertically downward to the ground. The specific positions and layout of each sensor are shown in **Figure 4**.

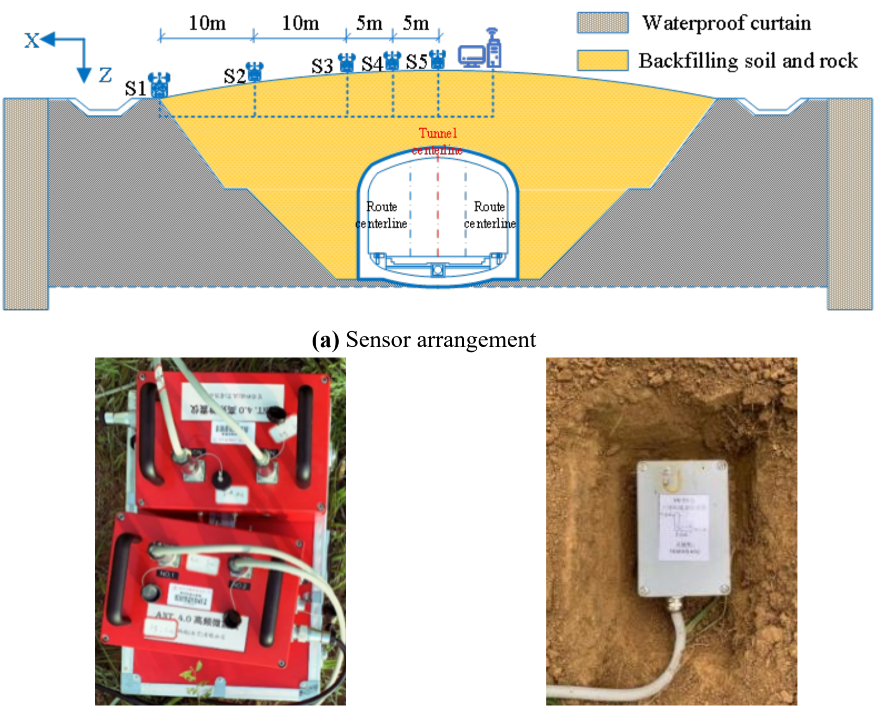

(a) Sensor arrangement

(b) High-frequency geological structure monitor **(c)** Vibration sensor

Figure 4. Sensor embedment.

The time-frequency characteristics of high-speed railway train vibration signals are significantly related to factors such as train marshalling, operating status, train type, and propagation medium characteristics. Four typical train numbers are selected from the 70 monitored train numbers. Since it is impossible to use a speedometer to determine the instantaneous speed of the train when passing the monitoring position, the train speed at the monitoring section was estimated from the spectral peak interval. The operating parameters of typical trains are shown in **Table 5**.

Table 5. Operation parameters of typical trains.

Train number	Train model	Marshalling	Operating speed (km/h)
G924	CRH380BG	8	285.14
G3604	CR400BF-G	8	217.54
G935	CR400BF-G	8	294.36
G902	CR400BF-G	16	215.30

3.2. VMD parameter adaptive decomposition

Taking the X-direction vibration signal measured by the S5 sensor under the action of the G924 train as an example, the adaptive decomposition of the vibration signal is performed. First, to ensure the integrity of the intercepted signal, when picking up the signal peak arrival time in the system, 50,000 sampling points (duration 5 s) are intercepted before and after the peak time to obtain the target interval of the target signal. At the same time, the starting point of the intercepted signal is specified as the time zero of the target signal. The time spectrum and frequency spectrum of the intercepted target signal are shown in **Figure 5**.

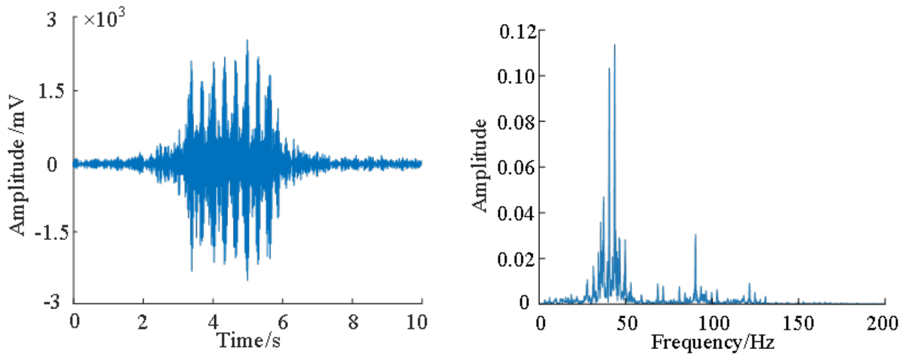

(a) X component time spectrum **(b)** X component frequency spectrum

Figure 5. Time-domain waveform and frequency spectrum of the target signal.

Since the number of sampling points of the target signal can reach 100,000, which has high requirements for the computing capacity of the computing equipment, the target signal is resampled to reduce the computational load. According to the Nyquist sampling theorem, when the minimum sampling frequency fs is greater than twice the maximum frequency fmax, the digital signal after sampling can relatively completely retain the effective information in the original signal, that is, the minimum sampling frequency satisfies Equation (14):

$$fs_{\min} \geq 2f_{\max} \tag{14}$$

Where, $fs_{\min}$ represents the minimum resampling frequency of the signal, Hz; $f_{\max}$ represents the maximum frequency of the signal, Hz.

It can be seen from **Figure 5b** that the main distribution range of the target signal frequency band is within 0–200 Hz. Therefore, the sampling frequency of the resampled signal is set to 500 Hz, its corresponding Nyquist frequency is 250 Hz, which can cover the main effective frequency range. Several studies [1–4] indicate that railway-induced ground and building vibrations are dominated by low-frequency components within 200 Hz. Therefore, resampling at 500 Hz will not affect the extraction of key information such as dominant frequency, mode energy, and propagation attenuation characteristics. The time spectrum and frequency spectrum of the target signal after resampling are shown in **Figure 6**. In the time spectrum, the signal peaks and waveforms before and after resampling are consistent. In the frequency spectrum, the frequency peaks and energy distribution range are almost unchanged, indicating that the resampled vibration signal effectively retains the effective components in the original signal, and its parameter optimization results can be used as the mode decomposition parameters of the target signal.

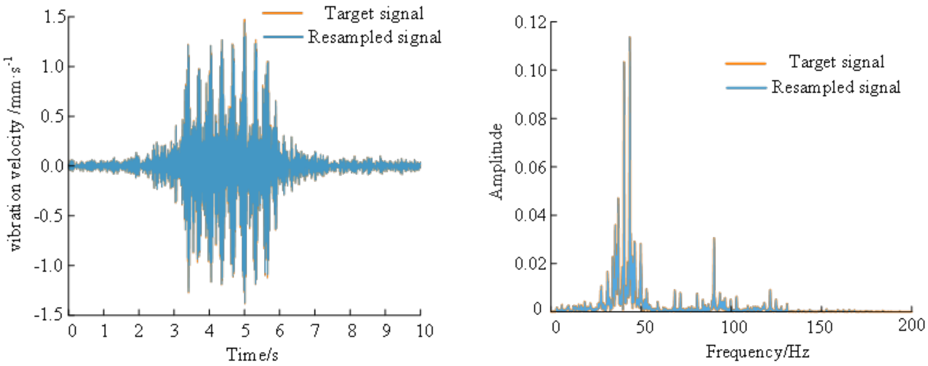

(a) Time spectrum of resampled signal **(b)** Frequency spectrum of resampled signal

Figure 6. Time-domain waveform and frequency spectrum of resampled signal.

3.3. Parameter optimization of high-speed railway train vibration signals

The obtained target signal is resampled according to the sampling theorem, and the optimal mode number K and penalty factor α of the VMD decomposition parameters of the resampled signal are optimized. The optimization parameters are shown in **Table 6** to determine the optimal parameter values for the target signal decomposition.

Table 6. SE-SSA parameters of the target signal.

Number of sparrow population n	Proportion of discoverers/ratio_PD	Safety value/ST	Range of mode number K	Range of penalty factor α
30	0.3	0.7	[3,15]	[1,10]

The convergence curve of the optimization process is shown in **Figure 7**. It can be seen that with the increase in the number of iterations, the fitness value shows phased stability. When the population at the 9th iteration, the X-direction vibration signal finally reaches the optimal fitness value of 0.4581 and tends to be stable. At this time, the optimal number of modes K and penalty factor α searched by SE-SSA are 15 and 5,317, respectively.

VMD is performed on the S5 vibration signal of the G924 train according to the determined number of modes and penalty factor to obtain mode components under different center frequencies. Taking the X-direction as an example, as shown in **Figure 8**, modes IMF1–IMF8 are high-frequency noise components with center frequencies of 1,971.19 Hz, 1,886.60 Hz, 1,809.15 Hz, 1,540.50 Hz, 1,336.70 Hz, 1,254.51 Hz, 1,194.45 Hz, and 616.82 Hz. The center frequencies are greater than 200 Hz, similar to high-frequency carriers, and the mode waveforms do not have the waveform characteristics of high-speed railway train vibration signals. Therefore, it is considered to eliminate the high-frequency noise components and retain the IMF that reflects the waveform of high-speed railway train vibration signals.

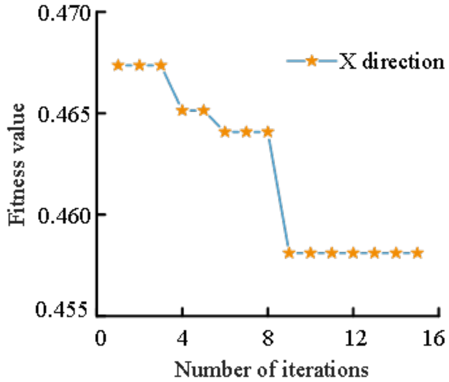

Figure 7. SE-SSA iteration curve of G924 train vibration signal (S5 sensor).

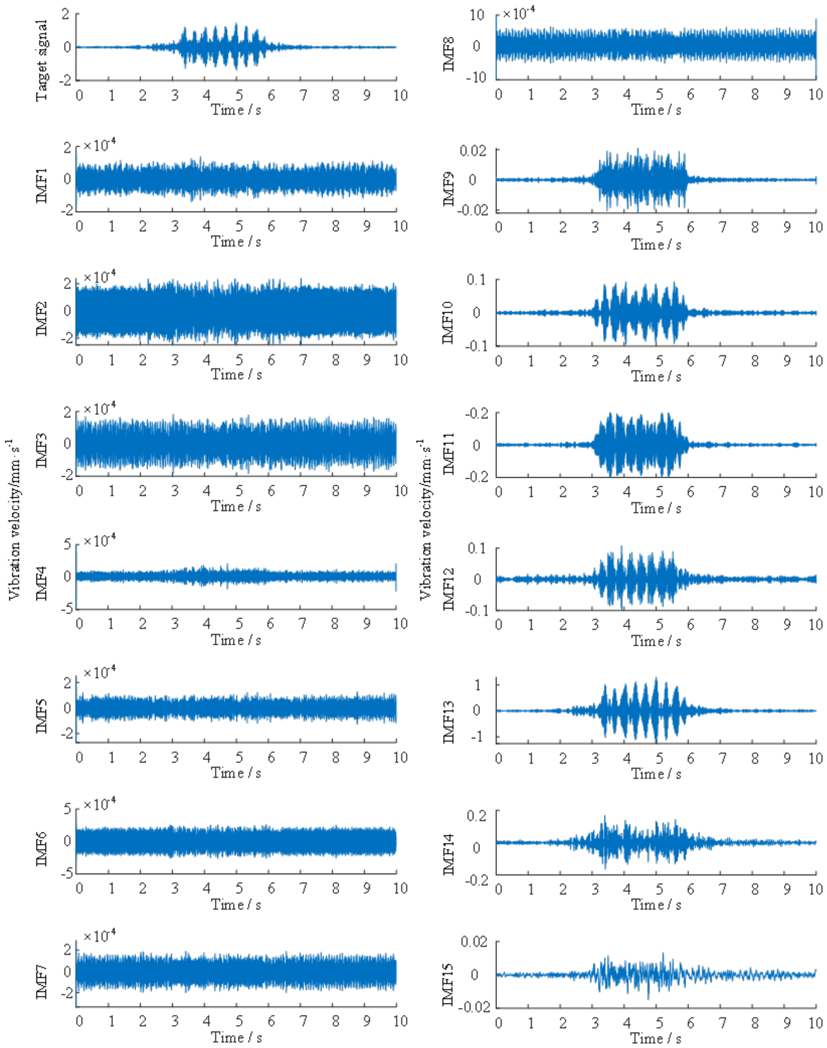

Figure 8. Mode components of the target signal for G924 train (S5 sensor X-direction).

Combining the mode waveform and center frequency characteristics in **Figure 8**, the mode components with center frequencies within 200 Hz are taken as effective modes to obtain the reconstructed high-speed railway train vibration signal $V(t)$. Then, parameter optimization is performed on $V(t)$ again, and VMD is performed on the reconstructed signal after obtaining the optimal number of modes and penalty factor, as shown in **Figure 9**. The optimization parameters are shown in **Table 7**.

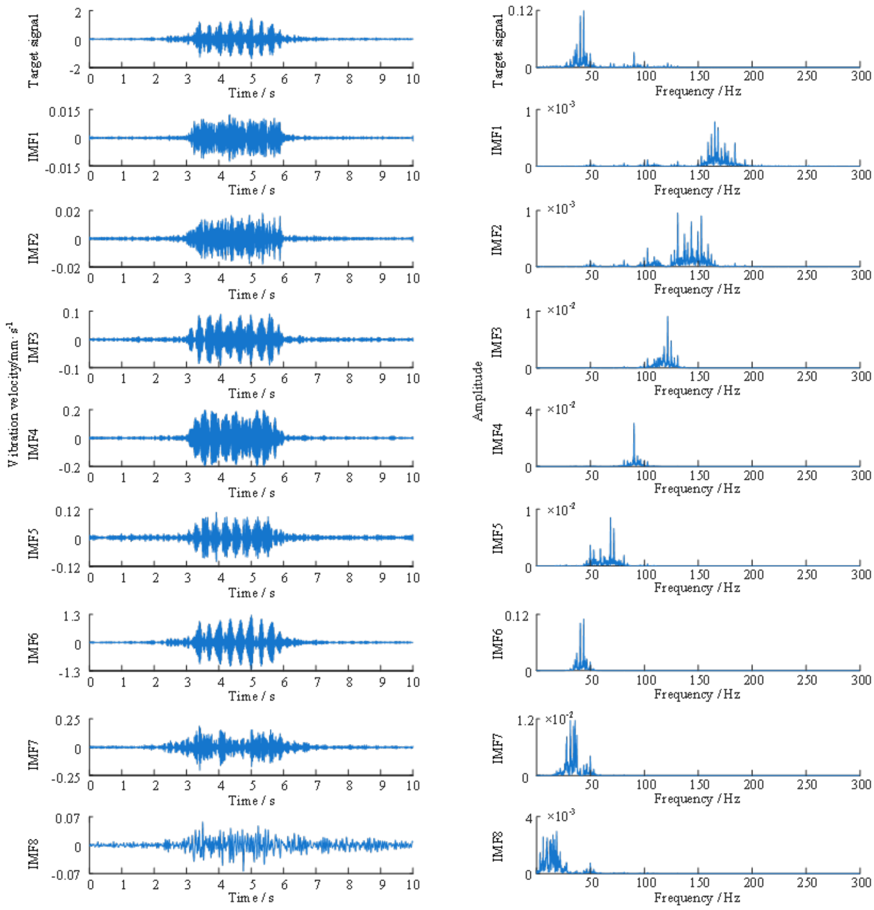

Figure 9. Mode components of the reconstructed signal for the G924 train (S5 sensor X-direction).

Table 7. VMD parameters optimization results of G924 train vibration signal.

Sensor	X-direction		Y-direction		Z-direction	
	Mode number *K*	**Penalty factor *α***	**Mode number *K***	**Penalty factor *α***	**Mode number *K***	**Penalty factor *α***
1	8	3,460	7	3,697	8	2,712
2	6	3,589	6	2,337	7	2,106
3	8	2,301	8	3,552	6	2,968
4	9	3,620	6	2,986	8	2,016
5	8	3,456	6	3,317	6	3,918

4. Energy-frequency characteristics of high-speed railway train vibration signals

4.1. Energy calculation of high-speed railway train vibration signals

Based on the general concept of signal energy in the field of signal and system analysis, high-speed railway train vibration signals can be regarded as vibration signals with certain regularity and limited duration. The signal energy over a finite time interval is calculated as follows in Equation (15) [26]:

$$E_S = \int_{t_1}^{t_2} |f(t)|^2 \, dt \tag{15}$$

Where, E_S is the signal energy; $f(t)$ is the signal function; t_1 and t_2 are the upper and lower time limits.

For the reconstructed high-speed railway train vibration signal $V(t)$, since the vibration data collection has a certain sampling interval $\Delta t = 1/fs$, the number of samples within the vibration signal time period is $N = (t_2 - t_1)/\Delta t = (t_2 - t_1)fs$. Based on Equation (15), the signal energy of the discrete time series $V(n)$ is as shown in Equation (16) [26]:

$$E_S = \sum_{n=1}^{N} V^2(n)\Delta t \tag{16}$$

Where, n is the sample point serial number; N is the number of samples.

The same method is used to calculate the energy of the vibration signal of each mode, so as to realize the quantitative calculation of the vibration energy and its energy at each frequency.

4.2. Energy-frequency distribution characteristics of high-speed railway train vibration signals

To quantitatively characterize the distribution law of mode energy of high-speed train vibration signals as a function of frequency, we take the G3604, G935, and G902 trains of CR400BF-G type high-speed EMU as research objects. An energy-frequency scatter plot is established with the effective mode center frequency of each measuring point as the abscissa and the corresponding mode energy as the ordinate, which is then fitted by a Gaussian function. The expression of the function is shown in Equation (17):

$$y = a \cdot e^{-\frac{(x-b)^2}{c^2}} \tag{17}$$

Where, a is the peak height of the fitting curve; b is the peak coordinate position of the fitting curve; c is the “bell-shaped” width of the fitting curve.

Curve fitting is performed under the condition of robust regression, the fitting accuracy is set to 10^{-8}, and the maximum number of function calculations and the maximum number of allowed iterations are set to 1,000. The Gaussian function fitting results of the component signal energy and frequency of high-speed railway train vibration signals in the X-, Y-, and Z-directions are shown in **Table 8**. The adjusted R^2 and Root Mean Square Error (RMSE) are used to represent the Gaussian fitting effect. The closer the adjusted R^2 value is to 1, and the closer the RMSE is to 0, the better the fitting effect. The relationship diagram between signal mode energy and frequency is drawn, as shown in **Figure 10**.

Table 8. Gaussian fitting results of energy and frequency for high-speed railway vibration signals.

Train information	Signal component	Gaussian parameter			Adjusted R^2	RMSE
		a	***b***	***c***		
G3604	X-direction	0.2164	51.89	11.18	0.9977	1.10×10^{-3}
	Y-direction	0.0206	66.62	26.32	0.9299	1.37×10^{-3}
	Z-direction	0.1693	53.40	10.22	0.9337	4.71×10^{-3}
G935	X-direction	0.4671	47.83	6.22	0.9722	1.74×10^{-3}
	Y-direction	0.0401	49.46	12.78	0.9993	1.72×10^{-3}
	Z-direction	0.6360	47.83	5.99	0.9706	1.54×10^{-2}
G902	X-direction	1.4890	44.86	8.21	0.9882	1.74×10^{-3}
	Y-direction	0.4071	45.60	8.34	0.9924	3.85×10^{-3}
	Z-direction	0.9160	46.08	6.21	0.9880	1.08×10^{-2}

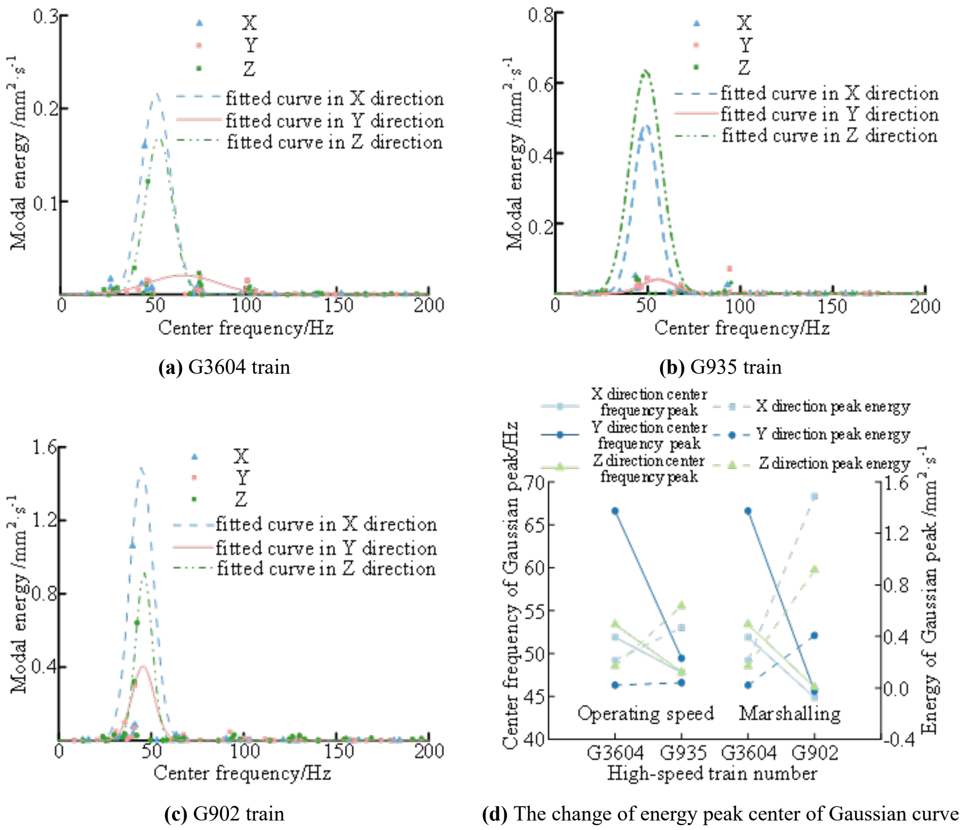

(a) G3604 train

(b) G935 train

(c) G902 train

(d) The change of energy peak center of Gaussian curve

Figure 10. Gaussian fitting of energy and frequency for high-speed railway vibration signal (G3604, G935, G902).

It can be seen from **Figure 10** that the relationship between the energy and frequency distribution of high-speed railway train vibration signals has typical Gaussian characteristics, and the mode energy value first increases and then decreases with the increase of the frequency value. The energy of each high-speed railway train vibration signal is mainly distributed in the frequency range of 35–60 Hz. Among them, the signal energy corresponding to each center frequency shows the characteristics of the largest X-direction component, followed by the Z-direction, and the smallest Y-direction. When a high-speed railway train is running, the contact between the train wheelset and the track is mainly lateral collision and vertical bounce, so the vibration perpendicular to the track direction is relatively strong, that is, the test ground survey line direction (X-direction) and the vertical direction (Z-direction), while the vibration in the running direction (Y-direction) is weak. Under the action of the same high-speed railway train, the peak energy center frequencies of the X component and Z component of the vibration signal are almost the same.

For trains G3604 (217.54 km/h) and G935 (294.36 km/h) with different operating speeds, with the increase of train speed, the peak energy in the X-direction increases by 0.2507 $mm^2 \cdot s^{-1}$, an increase of 115.9%; the peak energy in the Y-direction increases by 0.0195 $mm^2 \cdot s^{-1}$, an increase of 94.7%; the peak energy in the Z-direction increases by 0.4667 $mm^2 \cdot s^{-1}$, an increase of 275.7%. It is worth noting that the change in signal energy in the Y-direction is much smaller than that in the X- and Z-directions. The signal energy in the horizontal direction (X- and Y-directions) increases by about 1 time, while the energy in the vertical direction (Z-direction) increases by nearly 3 times, indicating that with the increase of train speed, the vertical bounce effect of the wheelset increases sharply, leading to a surge in vertical vibration energy. In addition, the increase in speed not only changes the vibration energy but also causes a systematic downward shift of the vibration source frequency characteristics. For the peak center frequency, the peak center frequency in the X-direction decreases by 4.06 Hz, a decrease of 7.8%; the peak center frequency in the Y-direction decreases by 17.16 Hz, a decrease of 25.8%; the peak center frequency in the Z-direction decreases by 5.21 Hz, a decrease of 9.8%.

For trains G3604 (8-car marshalling) and G902 (16-car marshalling) with different marshalling numbers, with the increase of train marshalling number, the peak energy in the X-direction increases by 1.2726$mm^2 \cdot s^{-1}$, an increase of 588.1%; the peak energy in the Y-direction increases by 0.3865 $mm^2 \cdot s^{-1}$, an increase of 1,876.2%; the peak energy in the Z-direction increases by 0.7467 $mm^2 \cdot s^{-1}$, an increase of 441.1%. It can be seen that the increase in the number of wheelset loads greatly improves the peak energy of the vibration signal. For the change of peak center frequency, the peak center frequency in the X-direction decreases by 7.03 Hz, a decrease of 13.5%; the peak center frequency in the Y-direction decreases by 21.02 Hz, a decrease of 31.6%; the peak center frequency in the Z-direction decreases by 6.96 Hz, a decrease of 13.12%. It can be seen that the peak center frequencies of vibration signals when the train is running with increased marshalling and increased speed have similar change trends: the frequency decrease of component signals perpendicular to the running direction (X- and Z-directions) is small, while the frequency decrease of Y-direction vibration signals is large.

In summary, both the increase in train speed and marshalling will multiply the energy of each component signal and concentrate it in the low-frequency band. The increase in train speed mainly enhances the vertical bounce effect of the wheelset, resulting in a surge in vertical vibration energy, while the increase in train marshalling mainly strengthens the lateral action of the wheelset, improving the X-direction vibration energy.

4.3. Energy-frequency variation characteristics of high-speed railway train vibration signals

To further explore the influence of train speed and marshalling number on the signal energy-frequency variation during the propagation and attenuation of high-speed railway train vibration signals, Gaussian function fitting is performed on the three-component signal energy and frequency generated by trains G3604, G935, and G902 at each sensor on the survey line. The fitting results are shown in **Table 9**. The fitting curves of each train number are displayed, taking the X-direction as an example, and the change relationships of peak energy and peak center frequency with the survey line are drawn, as shown in **Figures 11–13**.

Table 9. Gaussian fitting results of energy and frequency for high-speed railway vibration signals of each sensor.

Train number	Signal component	Sensor number	Gaussian parameter			Adjusted R^2	RMSE
			a	***b***	***c***		
G3604	X-direction	1	0.0182	48.56	14.57	0.932	1.20×10^{-3}
		2	0.0057	49.30	15.67	0.987	2.56×10^{-4}
		3	0.0472	48.90	11.80	0.994	1.91×10^{-4}
		4	0.0788	49.56	10.58	0.980	5.08×10^{-4}
		5	0.1977	51.65	12.66	0.998	1.99×10^{-3}
	Y-direction	1	0.0063	44.26	15.77	0.953	1.04×10^{-3}
		2	0.0023	36.04	17.72	0.990	9.78×10^{-5}
		3	0.0145	51.89	21.51	0.995	3.42×10^{-4}
		4	0.0195	59.10	14.47	0.838	7.90×10^{-4}
		5	0.0293	62.60	20.22	0.995	6.03×10^{-4}
	Z-direction	1	0.0026	45.00	13.45	0.935	3.33×10^{-4}
		2	0.0123	41.73	13.93	0.985	5.37×10^{-4}
		3	0.0298	43.09	14.68	0.976	1.56×10^{-3}
		4	0.0205	45.65	12.43	0.860	4.17×10^{-3}
		5	0.1551	54.21	13.70	0.994	3.65×10^{-3}
G935	X-direction	1	0.0509	42.52	13.52	0.977	2.97×10^{-3}
		2	0.0154	44.90	14.06	0.999	8.37×10^{-5}
		3	0.0254	48.01	9.13	0.917	2.28×10^{-3}
		4	0.0260	50. 05	16.66	0.984	1.05×10^{-3}
		5	0.4975	50.38	6.46	0.996	9.47×10^{-3}
	Y-direction	1	0.0405	42.64	12.97	0.996	9.15×10^{-4}
		2	0.0177	47.24	13.10	0.998	2.36×10^{-4}
		3	0.0368	48.01	14.32	0.992	1.10×10^{-3}
		4	0.0213	46.11	12.17	0.788	3.98×10^{-3}
		5	0.0443	49.14	17.41	0.999	4.43×10^{-3}
	Z-direction	1	0.0412	42.55	12.13	0.999	2.82×10^{-4}
		2	0.0391	44.00	10.97	0.937	3.55×10^{-3}
		3	0.0471	42.36	13.62	0.990	1.72×10^{-3}
		4	0.0227	45.01	14.15	0.952	1.24×10^{-3}
		5	0.6374	49.03	9.96	0.996	1.39×10^{-2}
G902	X-direction	1	0.1070	37.63	7.32	0.997	1.83×10^{-3}
		2	0.0747	40.53	10.92	0.987	2.99×10^{-3}
		3	0.0572	42.55	10.26	0.930	2.74×10^{-3}
		4	0.0392	45.82	16.51	0.881	3.88×10^{-3}
		5	1.1590	48.58	8.28	0.999	4.48×10^{-3}
	Y-direction	1	0.0201	43.35	11.91	0.998	2.54×10^{-4}
		2	0.0778	45.12	13.34	0.992	2.39×10^{-3}
		3	0.0242	40.65	11.95	0.958	1.71×10^{-3}
		4	0.2654	46.22	5.11	0.999	1.83×10^{-3}
		5	0.4346	48.18	11.80	0.973	1.76×10^{-2}
	Z-direction	1	0.0173	36.79	6.64	0.964	1.02×10^{-3}
		2	0.0288	39.65	8.52	0.929	2.47×10^{-3}
		3	0.0321	40.44	10.00	0.697	6.71×10^{-3}
		4	0.0526	45.43	16.14	0.821	5.45×10^{-3}
		5	0.8533	47.61	9.69	0.991	2.34×10^{-2}

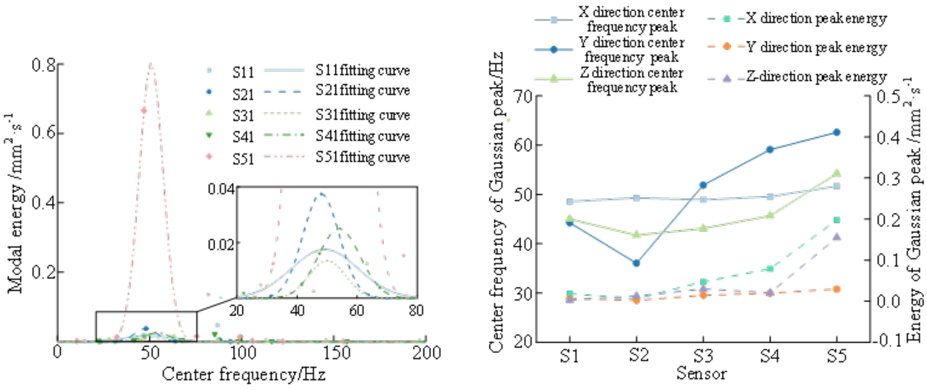

(a) G3604-X-direction **(b)** Gaussian fitting curve peak change

Figure 11. Gaussian fitting of energy and frequency for the G3604 train vibration signal.

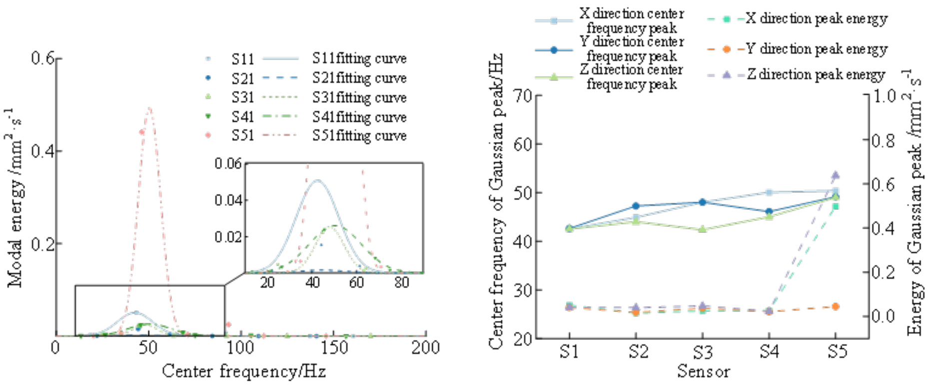

(a) G935-X-direction **(b)** Gaussian fitting curve peak change

Figure 12. Gaussian fitting of energy and frequency for G935 train vibration signal.

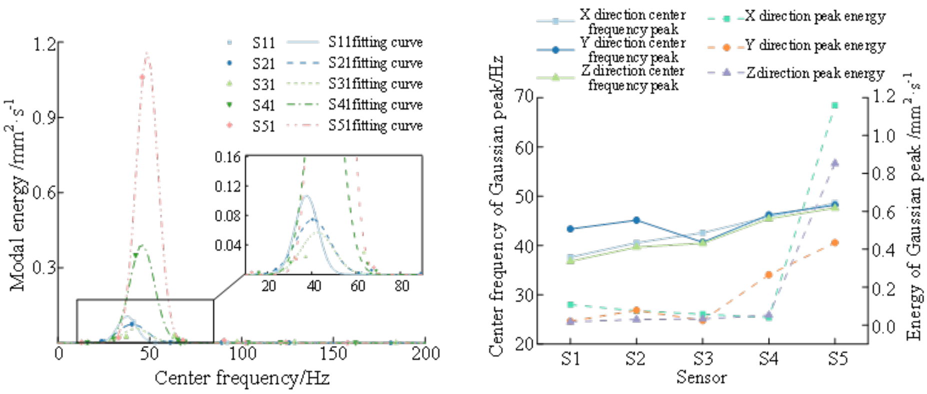

(a) G902-X-direction **(b)** Gaussian fitting curve peak change

Figure 13. Gaussian fitting of energy and frequency for G902 train vibration signal.

According to the fitting results of the energy and frequency of high-speed railway train vibration signals, the effective mode energy of each sensor generally exhibits a unimodal clustering characteristic with the variation of center frequency. The Gaussian function can well characterize the energy–frequency distribution law. According to the fitting results, the adjusted R^2 of all fitted curves is greater than 0.6, and more than 95% of the measuring points yield an adjusted R^2 above 0.8. This indicates that the adopted fitting form possesses good consistency across different measuring points and directions. Since the S5 sensor is closest to the running line, the peak values of the vibration signal curves of different train numbers at the S5 sensor are the largest. When reaching the S4 sensor, the signal energy attenuates sharply, and then the attenuation degree slows down. The vibration signal energy in each direction shows different degrees of attenuation, and there is a local increase phenomenon in the far-field range. Due to the difference in wave impedance of the medium in each direction during the propagation of vibration signals, the energy of vibration signals in different directions shows obvious differentiation, which is specifically manifested in that the peak energy of vibration signals in the X-direction and Z-direction is significantly higher than that in the Y-direction, that is, the vibration intensity perpendicular to the train running direction is higher than that parallel to the running direction.

It can be seen from the analysis of **Figure 11** and **Table 9** that under the action of train G3604, the peak center frequency of the X-direction component signal is concentrated around 50 Hz, showing a slight attenuation with the increase of propagation distance. The signal peak energy attenuates rapidly between S5 and S4, from 0.1977 $mm^2 \cdot s^{-1}$ to 0.0788 $mm^2 \cdot s^{-1}$, with a direct decrease of 60%. When the vibration propagates to the S2 and S1 sensors, the signal energy decrease exceeds 90%. The peak center frequency distribution of the Y-direction component signal is scattered in the range of 35–65 Hz, showing a decreasing trend from near to far. The signal peak energy also shows an attenuation trend, but due to the small overall energy in this direction, the attenuation rate is relatively slow. Between S5 and S4, the signal peak energy decreases from 0.0293 $mm^2 \cdot s^{-1}$ to 0.0195 $mm^2 \cdot s^{-1}$, a decrease of 33.4%. When reaching the S2 sensor, the decrease exceeds 90%, and there is an energy fluctuation phenomenon. Except for the S5 sensor with a peak center frequency of 54.21 Hz, the peak center frequencies of the Z-direction component signal are concentrated between 40 and 45 Hz, and the peak center frequency shows an attenuation trend. The signal peak energy between S5 and S4 decreases from 0.1551 $mm^2 \cdot s^{-1}$ to 0.0205 $mm^2 \cdot s^{-1}$, a decrease of 86.8%, with rapid attenuation, and then the attenuation slows down. The decrease of the S3-S1 sensors gradually decreases from 80.8% and 92.1% to 98.3%.

It can be seen from the analysis of **Figure 12** and **Table 9** that under the action of train G935, the peak center frequencies in the three directions are concentrated between 40–50 Hz, showing a decreasing trend with the increase of propagation distance, with local fluctuations. The peak energy of the X-direction component signal has been greatly attenuated at the S4 sensor, from 0.4975 $mm^2 \cdot s^{-1}$ to 0.0260 $mm^2 \cdot s^{-1}$, a decrease of 94.8%, with rapid attenuation, and then the attenuation becomes gentle, with the attenuation amplitude all above 90%. A local energy increase phenomenon occurs at the S1 sensor. Due to the low overall energy level of the peak energy of the Y-direction component signal, the attenuation amplitude is low, and it only decreases by 51.9% and 60.0% at the S4 and S2 sensor positions. The signal energy in this direction shows a fluctuating attenuation characteristic. The peak energy of the Z-direction component signal decreases from 0.6374 $mm^2 \cdot s^{-1}$ at the S5 sensor to 0.0227 $mm^2 \cdot s^{-1}$ at the S4 sensor, a decrease of 96.4%. The signal energy of the subsequent sensors recovers slightly, but the decrease is all above 90%, showing a stable change characteristic.

From the perspective of substantive differences and commonalities in energy propagation, train operating speed is a key variable affecting near-field energy characteristics. Due to the higher speed of train G935 294.36 km/h, the lateral collision force and vertical bounce force of the wheel-rail system are significantly greater than those of train G3604 217.54 km/h, directly leading to a significant increase in near-field (S5 sensor, adjacent to the tunnel center line) vibration energy in the X-direction (perpendicular to the track) and Z-direction (vertical direction). At the same time, the near-field (S5–S4) energy attenuation rate of train G935 is also faster, reflecting that the initial dissipation of higher energy vibration in artificial fill is more intense. However, the two trains show certain commonalities in the far-field section (S4–S1). Regardless of the differences in initial speed and near-field energy, the far-field vibration energy is generally maintained at a low level, which demonstrates the strong dissipation effect of the overlying artificial fill of the shallow-buried tunnel on vibration energy.

For train G902 (16-car marshalling), it can be seen from the analysis of **Figure 13** and **Table 9** that the peak center frequencies in the X-direction (perpendicular to the track) and Z-direction (vertical direction) show an approximately linear attenuation with the increase of propagation distance, without obvious fluctuations, and the final frequency stabilizes at 35–50 Hz, reflecting the dispersion stability of vibration waves perpendicular to the train running direction. The Y-direction (parallel to the track) has no linear law and always fluctuates within 40–50 Hz, which may be related to the stronger periodic disturbance of the wheel-rail in the parallel direction. In terms of peak energy attenuation, the X- and Z-directions of the near-field S5 sensor (adjacent to the tunnel center line) reach 1.159 $mm^2 \cdot s^{-1}$ and 0.8533$mm^2 \cdot s^{-1}$ respectively, and drop sharply to 0.0392$mm^2 \cdot s^{-1}$ and 0.0526 $mm^2 \cdot s^{-1}$ when propagating to the S4 sensor, with an attenuation amplitude of nearly 95%, highlighting the strong dissipation characteristics of the near-field artificial fill; after entering the far-field (S4→S1), the X-direction energy slightly increases and the Z-direction slowly decreases, but the cumulative attenuation is more than 90%. The near-field (S5→S4) decrease of the Y-direction is only 38.9% (0.4346→0.2654 $mm^2 \cdot s^{-1}$), and the far-field shows fluctuating attenuation. Finally, the far-field energies in the three directions tend to be the same, dominated by medium dissipation.

Compared with the vibration signal characteristics of Train G3604 with 8-car marshalling, the vibration differences of Train G902 with 16-car marshalling are mainly reflected in three aspects. Firstly, the near-field vibration energy is significantly increased, and the vibration energy in the X-, Z-, and Y-directions monitored by the S5 sensor is all higher than that of Train G3604, which is attributed to the increased total wheelset load caused by the growth of train marshalling quantity, thereby enhancing the overall energy of wheel-rail lateral collision and vertical bounce excitation. Secondly, the two trains present distinct attenuation nodes and attenuation rates. The vibration energy in the X- and Z-directions of Train G902 rapidly decays to a low level at the S4 sensor, while that of Train G3604 only decreases to the same low level until reaching the S3 sensor, and Train G902 has a faster overall attenuation rate; specifically, the vibration energy in the X-direction of Train G902 attenuates by nearly 95%, while the corresponding attenuation amplitude of Train G3604 is only 60%. In the Y-direction, the vibration energy of Train G902 drops to a low level at the S3 sensor, whereas Train G3604 needs to propagate to the S4 sensor to complete effective attenuation.

Thirdly, Train G902 shows a more concentrated frequency distribution accompanied by an obvious low-frequency offset. Its peak center frequencies are stably concentrated in the range of 35–50 Hz, which is integrally 5 Hz lower than the corresponding frequency distribution of Train G3604. Meanwhile, the linear attenuation characteristics of vibration energy in the X- and Z-directions of Train G902 are more prominent, which is reasonably speculated to be closely related to the reduction of wheel-rail contact frequency induced by the multi-car long marshalling operation condition of the train. It should be noted that the far-field vibration energy does not exhibit strictly monotonic attenuation at all measuring points and in all directions, and local fluctuations or slight rebound phenomena occur in some directions. For example, the Y-direction of Train G902 shows distinct fluctuating attenuation characteristics. This may be related to the heterogeneity of the overlying fill soil, the wave impedance difference at the interface between the soil mass and the tunnel structure, as well as wave reflection, scattering, and local superposition. Overall, the far-field vibration energy remains at a low level, indicating that the overlying fill soil has a strong dissipation effect on the vibration energy induced by train operation.

Based on the above results of energy–frequency distribution and propagation attenuation, the method proposed in this paper can provide a reference for the monitoring and evaluation of high-speed railway vibration in shallow-buried tunnel sections. In field monitoring, the SE-SSA-VMD method can extract effective modes reflecting train excitation characteristics from high-noise and non-stationary vibration signals, which is applicable to signal preprocessing prior to the calculation of dominant frequency, energy, and attenuation indicators. For vibration assessment in sensitive areas, the identified main energy frequency band of 35–60 Hz can be regarded as the key evaluation range for sensitive targets, including residential districts, schools, hospitals, and precision instrument buildings. In terms of vibration reduction design, the increase in running speed and train marshalling imposes differentiated effects on vibration energy in various directions, suggesting that the vibration mitigation strategy for shallow-buried tunnel sections should specify key directions and target frequency bands according to actual operating conditions. Meanwhile, the attenuation law of vibration energy along the measuring line can support the layout of monitoring points as well as the determination of key near-field control scope and far-field protection scope.

5. Conclusion

This study proposes using Sample Entropy (SE) as the fitness function, combined with the Sparrow Search Algorithm (SSA), to adaptively optimize the key parameters (number of modes K and penalty factor α) in Variational Mode Decomposition (VMD), constructing the SE-SSA-VMD vibration signal analysis method, and applying it to the analysis of surface vibration signals above shallow-buried high-speed railway tunnels. The main conclusions are as follows:

(1) The SE-SSA-VMD method can effectively overcome the mode mixing and parameter dependence problems in traditional mode decomposition and realize the accurate separation of noisy high-speed railway train vibration signals. In

the 7 dB low SNR benchmark test, this method effectively suppresses mode mixing and solves the inherent defects of traditional EMD and EWT; compared with mainstream PSO-VMD, it achieves better decomposition accuracy with an average center frequency error as low as 0.10 Hz. It also accurately identifies dominant frequency components in the 5–15 dB SNR range, with maximum center frequency error below 0.25 Hz at 5 dB, showing excellent robustness for complex vibration signal processing of shallow-buried high-speed railway tunnels. This method avoids subjective interference from manual parameter selection, improves the objectivity and reliability of signal decomposition, and provides a new way to extract effective wheel-rail vibration components from a strong noise background.

(2) The effective mode energy of high-speed railway train vibration signals on the surface above shallow-buried tunnels is mainly concentrated in the 35–60 Hz frequency band, whose energy-frequency relationship can be well characterized by a Gaussian function, with more than 95% of measurement points yielding an adjusted R^2 above 0.8 and 93% having a root mean square error (RMSE) lower than 1×10^{-2}, demonstrating that the energy distribution within this band exhibits prominent unimodal aggregation features and satisfactory consistency across measurement points. Measured data show that the spatial distribution of vibration energy has obvious anisotropy. Lateral collision and vertical bounce dominate the wheel-rail interaction. The peak energy corresponding to each center frequency shows the characteristics that the component perpendicular to the track direction (X-direction) is the largest, the vertical direction (Z-direction) is the second, and the component parallel to the track direction (Y-direction) is the smallest. Under the action of the same high-speed railway train, the peak energy center frequencies of the X and Z components are basically the same.

(3) Train operating speed and marshalling number are key factors affecting vibration energy and dominant frequency characteristics. The increase in train speed will enhance the vertical bounce effect of the wheelset, thereby significantly increasing the Z-direction vibration energy. Increasing train marshalling will strengthen the lateral action of the wheelset, increasing the X-direction vibration energy. Both increasing train speed and marshalling will cause the peak center frequency to shift to low frequencies. Among them, the peak center frequency of the Y-direction component signal has the largest decrease, while the peak center frequencies of the X- and Z-direction component signals have smaller decreases.

(4) For high-speed railway train vibration signals on the surface above shallow-buried tunnels, their energy, frequency, and propagation attenuation laws are significantly affected by train speed, marshalling, and propagation direction. An increase in train speed (from 217.54 km/h to 294.36 km/h) or marshalling (from 8-car marshalling to 16-car marshalling) enhances the X- and Z-direction vibration energy in the near-field (e.g., S5 sensor) and accelerates the near-field energy attenuation. In terms of propagation direction, the vibration energy in the X- and Z-directions is always significantly higher than that in the Y-direction. The peak center frequencies of the X- and Z-directions show a linear attenuation with the increase of propagation

distance, while the peak center frequency of the Y-direction fluctuates within a specific frequency band. Dominated by the strong dissipation characteristics of the overlying artificial fill, the far-field (from S4 to S1 sensors) vibration energy generally attenuates by more than 95%, and finally the energies of the X-, Y-, and Z-directions tend to be consistent. This characteristic is not affected by train speed, marshalling number, or propagation direction.

Author contributions: Conceptualization, LZ and BJ; methodology, LZ, BJ, KZ and ZZ; validation, KZ, ZZ and SD; formal analysis, LZ, KZ, ZZ and SD; investigation, KZ; data curation, KZ; writing—original draft preparation, LZ and KZ; writing—review and editing, BJ, ZZ and SD; funding acquisition, LZ and BJ. All authors have read and agreed to the published version of the manuscript.

Funding: This research was funded by LIAONING PROVINCIAL RESEARCH FOUNDATION FOR BASIC RESEARCH, grant number 2022JH2/101300227; NATIONAL NATURAL SCIENCE FOUNDATION OF CHINA, grant number 52404082; YOUTH PROJECT OF BASIC SCIENTIFIC RESEARCH PROJECT FOR UNIVERSITIES OF EDUCATIONAL DEPARTMENT OF LIAONING PROVINCE, grant number LJ212510147045; OPEN FOUNDATION OF KEY LABORATORY OF SAFE AND EFFECTIVE COAL MINING, MINISTRY OF EDUCATION (ANHUI UNIVERSITY OF SCIENCE AND TECHNOLOGY), grant number JYBSYS202308; LIAONING BAIQIANWAN TALENTS PROGRAM, grant number 2021921023.

Institutional review board statement: Not applicable.

Informed consent statement: Not applicable.

Data availability statement: All data used in this paper will be made available on request.

Conflict of interest: The authors declare no competing interests.

AI use statement: During the preparation of this manuscript, the authors used DeepSeek solely for language refinement. No AI tools were used for data analysis, interpretation, or generation of scientific content. All outputs were critically reviewed and edited by the authors. The authors take full responsibility for the integrity and accuracy of the work.

References

1. Zhou Z, Jia B, Yuan W, et al. Vibration response prediction and vibration safety assessment method for building structures around viaducts under the action of high-speed railway trains. Construction and Building Materials. 2024; 422: 135877. doi: 10.1016/j.conbuildmat.2024.135877
2. Connolly DP, Kouroussis G, Laghrouche O, et al. Benchmarking railway vibrations—Track, vehicle, ground and building effects. Construction and Building Materials. 2015; 92: 64–81. doi: 10.1016/j.conbuildmat.2014.07.042
3. Thompson DJ, Kouroussis G, Ntotsios E. Modelling, simulation and evaluation of ground vibration caused by rail vehicles. Vehicle System Dynamics. 2019; 57(7): 936–983. doi: 10.1080/00423114.2019.1602274
4. Gao X, Yi Q, Lei J, et al. Experimental study on the characteristics of vibration energy propagation in the subway turnout area. Construction and Building Materials. 2023; 409: 134210. doi: 10.1016/j.conbuildmat.2023.134210
5. Degen KG, Behr W, Grütz H-P. Investigations and results concerning railway-induced ground-borne vibrations in

Germany. Journal of Sound and Vibration. 2006; 293(3–5): 865–872. doi: 10.1016/j.jsv.2005.12.021
6. Khan MR, Dasaka SM. Characterisation of High-Speed Train Vibrations in Ground Supporting Ballasted Railway Tracks. Transportation Infrastructure Geotechnology. 2020; 7(1): 69–84. doi: 10.1007/s40515-019-00091-w
7. Li M, Ma M, Cao Z, et al. Dynamic response analysis of train-induced vibration impact on the Probhutaratna pagoda in Beijing. Earthquake Engineering and Engineering Vibration. 2021; 20(1): 223–243. doi: 10.1007/s11803-021-2016-9
8. Lei J, Gao X, Wang Y, et al. Vibration characteristics of subway turnout area during vehicle deceleration and assessment of the model accuracy. Measurement. 2024; 231: 114566. doi: 10.1016/j.measurement.2024.114566
9. Yi Q, Zhao L, Gao Y, et al. Experimental study on characteristics of vibration source and effect of vibration reduction measures in turnout of urban rail transit. Journal of Railway Science and Engineering. 2024; 21(5): 1854–1865. Available online: https://doi.org/10.19713/j.cnki.43-1423/u.T20231144 (in Chinese)
10. Zhang B, Wan S, Zhao X, et al. Instantaneous rotational frequency estimation and fault diagnosis for rotating machinery based on multi-component short-time Fourier transform. Measurement. 2025; 253: 117565. doi: 10.1016/j.measurement.2025.117565
11. Li D, Wang Y, Yan WJ, et al. Acoustic emission wave classification for rail crack monitoring based on synchrosqueezed wavelet transform and multi-branch convolutional neural network. Structural Health Monitoring. 2021; 20(4): 1563–1582. doi: 10.1177/1475921720922797
12. Tian J, Tian Z, Zhang M, et al. A novel identification method of microseismic events based on empirical mode decomposition and artificial neural network features. Journal of Applied Geophysics. 2024; 222: 105329. doi: 10.1016/j.jappgeo.2024.105329
13. Mounir N, Ouadi H, Jrhilifa I. Short-term electric load forecasting using an EMD-BI-LSTM approach for smart grid energy management system. Energy and Buildings. 2023; 288: 113022. doi: 10.1016/j.enbuild.2023.113022
14. Gao Z, Zheng J, Pan H, et al. Adaptive generalized empirical wavelet transform and its application to fault diagnosis of rolling bearing. Measurement. 2025; 249: 116958. doi: 10.1016/j.measurement.2025.116958
15. Dragomiretskiy K, Zosso D. Variational Mode Decomposition. IEEE Transactions on Signal Processing. 2014; 62(3): 531–544. doi: 10.1109/TSP.2013.2288675
16. Jia H, Cao P, Liang T, et al. Short-time variational mode decomposition. Signal Processing. 2026; 238: 110203. doi: 10.1016/j.sigpro.2025.110203
17. Ren H, Liu W, Shan M, et al. A new wind turbine health condition monitoring method based on VMD-MPE and feature-based transfer learning. Measurement. 2019; 148: 106906. doi: 10.1016/j.measurement.2019.106906
18. Cai G, Wang L, Yang D, et al. Harmonic Detection for Power Grids Using Adaptive Variational Mode Decomposition. Energies. 2019; 12(2): 232. doi: 10.3390/en12020232
19. Lian J, Liu Z, Wang H, et al. Adaptive variational mode decomposition method for signal processing based on mode characteristic. Mechanical Systems and Signal Processing. 2018; 107: 53–77. doi: 10.1016/j.ymssp.2018.01.019
20. Gu R, Chen J, Hong R, et al. Incipient fault diagnosis of rolling bearings based on adaptive variational mode decomposition and Teager energy operator. Measurement. 2020; 149: 106941. doi: 10.1016/j.measurement.2019.106941
21. Zhang XL, Jia RS, Lu XM, et al. Identification of blasting vibration and coal-rock fracturing microseismic signals. Applied Geophysics. 2018; 15(2): 280–289. doi: 10.1007/s11770-018-0682-9
22. Yang K, Wang G, Dong Y, et al. Early chatter identification based on an optimized variational mode decomposition. Mechanical Systems and Signal Processing. 2019; 115: 238–254. doi: 10.1016/j.ymssp.2018.05.052
23. Xue J, Shen B. A novel swarm intelligence optimization approach: sparrow search algorithm. Systems Science & Control Engineering. 2020; 8(1): 22–34. doi: 10.1080/21642583.2019.1708830
24. Zhang X, Liang J, Zhang X, et al. Combined Model for Ultra Short-term Wind Power Prediction Based on Sample Entropy and Extreme Learning Machine. Proceedings of the CSEE. 2013; 33(25): 33–40+8. Available online: https://doi.org/10.13334/j.0258-8013.pcsee.2013.25.012 (in Chinese)
25. Liang B, Luo H, Sun C. Simulated study on vibration load of high speed railway. Journal of the China Railway Society. 2006; 28(4): 89–94. (in Chinese)
26. Zhou L. Study on Microseismic Wave Propagation Velocity Model and Energy Frequency Characteristics of Overburden Rock in Mined-Out Area [PhD Thesis]. Liaoning Technical University; 2022. Available online: https://doi.org/10.27210/d.cnki.glnju.2022.000889 (in Chinese)